energies

MDPI

Article

Numerical Simulation and Experimental Verification of the Atomization Characteristics of Gas–Liquid Two-Phase Impact Jet Nozzle Based on the VOF-DPM Coupling Method

Renjie Wu [1], Jianhua Zhao [1,*], Zhaowen Wang [2], Kun Yang [1], Lei Zhou [1], Yuwei Zhang [1] and Qiguang Wang [2]

[1] Naval University of Engineering, Wuhan 430030, China; m25182413@nue.edu.cn (R.W.); 18664329187@163.com (K.Y.); 15345811275@163.com (L.Z.); rei2382025@163.com (Y.Z.)
[2] School of Energy and Power Engineering, Huazhong University of Science and Technology, Wuhan 430074, China; wangzhaowen@hust.edu.cn (Z.W.); 19174031063@163.com (Q.W.)
* Correspondence: zhaojh402@sina.com

Abstract

Exhaust piping in diesel engines is subject to severe thermal stress arising from high-temperature, high-pressure gas flows, and spray cooling with atomizing nozzles has become a widely adopted method to safeguard structural reliability. However, at present, the understanding of the spray fragmentation mechanism of two-phase flow under low inlet pressure is still not comprehensive. This study establishes a three-dimensional model of a gas–liquid impinging-jet nozzle and applies a coupled Volume-of-Fluid to Discrete-Phase-Model (VOF–DPM) approach to resolve the liquid breakup process in detail. High-speed imaging experiments were carried out to validate the numerical results. Orthogonal tests were conducted at five pressure levels for both gas and water—0.28, 0.24, 0.20, 0.16, and 0.12 MPa—producing 25 data pairs of spray cone angle and Sauter Mean Diameter (SMD). Within the 0–0.3 MPa air inlet pressure range explored here, raising the pressure consistently reduced the SMD and widened the cone angle, although both trends weakened as the pressure increased. Water inlet pressure exhibited a nonlinear influence, with local extrema appearing in the higher-pressure region. The overall SMD reached a minimum of 34.12 μm and a maximum of 149.04 μm. Using these 25 data points, a genetic algorithm was employed to optimize the pressure ratio under the constraint of total hydraulic power, yielding optimization strategies for different power budgets. An additional outcome of the simulation was the identification of a structural weakness: by reshaping the original flat impingement surface into a full conical surface, atomization quality improved by 29.36% under identical boundary conditions. These findings clarify the atomization mechanism of gas–liquid impinging jets under low inlet pressure and offer practical guidance for nozzle optimization.

Keywords: VOF-DPM; two-phase flow nozzle; atomization performance; structure optimization

Academic Editor: Andrea De Pascale

Received: 18 May 2026
Revised: 4 June 2026
Accepted: 7 June 2026
Published: 12 June 2026

1. Introduction

Exhaust piping systems operate continuously in harsh environments characterized by high temperature, high pressure, and cyclic thermal loading [1]. These conditions are the primary factors that induce thermal stress concentration and threaten structural integrity. Thermal stresses mainly develop when the thermal expansion or contraction of a material is geometrically constrained, and they become particularly pronounced under transient temperature loads, making such components highly susceptible to fatigue damage. Higher operating parameters and more frequent start–stop operations accelerate the fatigue degradation of these components, which is typically a localized phenomenon caused by thermomechanical fatigue [2]. Among various technical approaches, spray cooling systems that employ nozzles to achieve efficient atomization for heat absorption and pollutant removal—benefiting from extremely high heat transfer coefficients and good temperature uniformity—are regarded as one of the most promising solutions to the structural challenges posed by thermal stresses in exhaust piping [3–6]. The heat transfer mechanisms of spray cooling are highly complex, involving multiple coupled processes such as droplet spreading, film formation, evaporation, and convective heat transfer after droplets impinge on a hot wall [7–10]. Spray cooling performance depends on a chain of interconnected physical processes. The first link is atomization quality, which determines the droplet size distribution, velocity field, and spatial dispersion of the spray. These atomization parameters govern the second link, namely droplet impingement on the hot wall, liquid film formation, and film spreading behaviour. The third link encompasses the thermal response of the wall, including evaporative cooling, possible nucleate or transition boiling, and the resulting heat flux. Mudawar [11] reviewed the full chain from spray generation to two-phase heat transfer and showed that droplet size and impact density are the dominant upstream parameters controlling cooling performance in high heat flux applications. Liang et al. [12] directly measured the transient heat transfer induced by spray impingement on a piston surface and demonstrated that changes in spray characteristics produce measurable and predictable changes in wall heat flux. Raveshi et al. [13] further showed that fluid properties and surface wetting conditions critically modulate the boiling heat transfer coefficient. The present study focuses on the first link of this chain. As the initial link in the entire heat transfer chain, the droplet size, velocity, and spatial distribution produced by nozzle atomization directly determine the morphology of the cooling liquid film and the evolution of the thermal boundary layer, and therefore play a decisive role in the ultimate cooling performance [14]. Consequently, precisely controlling atomization characteristics and achieving active design of the droplet size distribution are crucial for enhancing the efficiency and reliability of spray cooling systems [15].

Impinging jet atomization, particularly gas–liquid coaxial jet impingement onto a wall, combines the shear breakup of the coaxial jet with the spreading dynamics of the jet impacting a solid surface. The physical process can be broadly divided into several stages: a central low-speed liquid jet is enveloped by a surrounding annular high-speed gas stream, creating a strong velocity gradient at the gas–liquid interface that triggers Kelvin–Helmholtz instability [16], which is the primary driving force for surface wave growth and primary breakup; subsequently, the initially deformed liquid column or ligaments impinge on the solid wall directly below, generating a high-pressure stagnation zone that drives the liquid to spread radially into a thin film; the rim of this liquid film, under the continuous impingement and shear of the subsequent flow, is torn by the combined action of Rayleigh–Taylor instability and surface tension, forming ligaments and large liquid blobs [17–19]; and, finally, these irregular large-scale blobs undergo secondary atomization under further aerodynamic forces, breaking up into finer droplet clusters. These transient processes, occurring at millimeter to micrometer scales, place extremely high demands on both experimental measurement and theoretical modeling.

Because atomization involves complex gas–liquid two-phase interactions and cross-scale physical phenomena such as liquid film instability, ligament breakup, and secondary droplet breakup, it is difficult to thoroughly reveal the underlying mechanisms by experimental means alone, and such experiments are also costly and time-consuming. Therefore, Computational Fluid Dynamics (CFD) numerical simulation has become an important method for investigating nozzle atomization processes [20–22]. Regarding numerical methodologies, the Volume of Fluid (VOF) method is based on an Eulerian–Eulerian framework and captures the evolution of the gas–liquid interface by solving the volume fraction transport equation, which makes it suitable for simulating liquid film formation and primary atomization inside the nozzle [23,24]. However, the VOF method requires a grid resolution much finer than the droplet size, leading to prohibitively high computational cost when the number of droplets is very large, making it difficult to simulate the motion of the dilute droplet swarm after secondary atomization. The Discrete Phase Model (DPM), based on an Eulerian–Lagrangian framework, treats droplets as discrete particles and tracks their trajectories by solving the particle equation of motion, and is thus suitable for dilute spray simulations [25]; however, it cannot capture the continuous interfacial evolution of the liquid film.

In recent years, the coupled VOF–DPM approach has attracted considerable attention. This method employs the VOF method to resolve the continuous liquid film region, and automatically converts liquid blobs into DPM particles once certain breakup criteria are satisfied, thereby achieving a coupled simulation of the entire process from primary to secondary atomization. Studies have demonstrated that the VOF–DPM-coupled method can effectively reproduce atomization phenomena such as liquid film instability, ligament breakup, and secondary droplet breakup, and can accurately predict the droplet size distribution during the atomization process.

Although the VOF–DPM method has been applied to investigations of various atomizers, such as pressure-swirl nozzles and air-assisted nozzles [26–29], combined numerical and experimental studies on the specific configuration of gas–liquid coaxial jet impingement onto a wall—which features a more complex geometry and more comprehensive flow mechanisms—remain relatively scarce. In particular, further quantitative analysis is needed to understand how operating parameters influence the formation and breakup of the wall film as well as the resulting droplet size distribution. Moreover, existing studies have mostly been conducted under conventional environmental conditions, and the understanding of impinging jet atomization under the inlet pressure generated by engine-driven pumps is still insufficient. To this end, the present work takes a gas–liquid coaxial impinging-jet nozzle intended for spray cooling as the research object. Based on the ANSYS Fluent 2022 R1 platform, a multiscale numerical simulation method that couples VOF and DPM in a two-way manner, combined with Adaptive Mesh Refinement (AMR) technology, is employed to perform a three-dimensional, high-fidelity transient simulation of the complete atomization process of such a nozzle. In this model, the VOF method accurately captures the gas–liquid interface evolution and primary film breakup in the Eulerian framework, while liquid blobs that satisfy prescribed size and shape criteria are dynamically converted into DPM particles in the Lagrangian framework to efficiently track the secondary atomization process. To validate the reliability of the numerical model, a spray visualization experimental platform was constructed. Using high-speed photography technology and a laser particle size analyzer, a systematic comparative study was conducted on SMD and spray cone angles. The simulation predictions agreed well with the experimental data, confirming that the numerical framework can accurately capture the impingement atomization characteristics. Using the validated model, a parametric study was then performed to investigate how different liquid and gas inlet pressure combinations affect atomization quality across the 0–0.3 MPa operating range. The interplay between aerodynamic shear force and liquid film inertia was examined, revealing that an optimal gas–liquid pressure combination exists, at which the overall SMD reaches its minimum. These results provide a theoretical basis for the optimal design of spray cooling nozzles and offer a clearer understanding of the physics behind impinging jet breakup.

https://doi.org/10.3390/en19122812

2. Theory and Methods

2.1. Basic Governing Equations

The physics of gas–liquid two-phase flow is governed by the conservation laws of mass and momentum. The present study considers a transient, three-dimensional, isothermal flow. The general form of the governing equations is as follows:

Continuity equation:

$$\frac{\partial \rho}{\partial t} + \nabla \cdot (\rho \vec{u}) = 0 \tag{1}$$

Momentum conservation equation:

$$\frac{\partial (\rho \vec{u})}{\partial t} + \nabla \cdot (\rho \vec{u} \vec{u}) = -\nabla P + \nabla \cdot \tau + F \tag{2}$$

In the above equations, $\vec{u}$ is the velocity vector; ρ is the fluid density; P is the pressure; τ is the stress tensor; and F represents the body force per unit volume, which includes gravity and other external forces.

2.2. Turbulence Model: Shear Stress Transport SST k-ω Model

Accurately predicting the strong shear layers, vortices, and separated flows in gas–liquid two-phase jets is crucial for simulating the atomization process. In this work, the Shear Stress Transport (SST) k-ω model proposed by Menter is adopted to close the Reynolds-averaged Navier–Stokes equations. This model employs a hybrid function to combine the standard k-ω model with the k-ε model, in order to accommodate the main flow field far from the wall. This zonal blending strategy makes the SST k-ω model particularly suitable for complex flows characterized by adverse pressure gradients, separation, and strong shear, such as the shear layer of the coaxial jet and the radially spreading flow after wall impingement investigated in this study.

The transport equations of the SST k-ω model are

$$\frac{\partial}{\partial t}(\rho k) + \frac{\partial}{\partial x_j}(\rho k u_j) = \frac{\partial}{\partial x_j}(\Gamma_k \frac{\partial k}{\partial x_j}) + G_k - Y_k \tag{3}$$

$$\frac{\partial}{\partial t}(\rho \omega) + \frac{\partial}{\partial x_j}(\rho \omega u_j) = \frac{\partial}{\partial x_j}(\Gamma_\omega \frac{\partial \omega}{\partial x_j}) + G_\omega - Y_\omega + D_\omega \tag{4}$$

where G_k is the production of turbulence kinetic energy due to mean velocity gradients, G_ω is the production of the specific dissipation rate, Y_k and Y_ω represent the dissipation of k and ω due to turbulence, Γ_k and Γ_ω are the effective diffusivities, and D_ω is the cross-diffusion term; ρ is the density; k is the turbulence kinetic energy; u_j is the mean velocity component; x_j is the spatial coordinate; and ω is the specific dissipation rat.

2.3. Multiphase Model: Volume of Fluid

The VOF method is a powerful approach for tracking the interface between immiscible fluids on a fixed Eulerian grid. It is based on solving a set of volume fraction equations. For the qth phase, the continuity equation for the volume fraction α_q is given by

$$\frac{\partial}{\partial t}(\alpha_q \rho_q) + \nabla \cdot (\alpha_q \rho_q u_q) = S_{\alpha_q} + \sum_{p=1}^{n} (\dot{m}_{pq} - \dot{m}_{qp}) \tag{5}$$

where $\dot{m}_{pq}$ represents the mass transfer from phase p to phase q. In the cold flow considered here, this term is zero. The volume fraction of the primary phase is obtained from the constraint $\sum_{q=1}^{n} \alpha_q = 1$. The material properties appearing in the continuity and momentum equations are computed as volume-fraction-weighted averages of the phase properties, e.g., $\rho = \alpha_l \rho_l + (1 - \alpha_l)\rho_g$.

To maintain a sharp and accurate gas–liquid interface, the volume fraction equation is discretized in time with an explicit scheme and in space using the Geometric Reconstruction scheme. This method assumes that the interface between two phases has a linear slope within each computational cell and uses this linear shape to compute the convective fluxes through the cell faces, thereby minimizing numerical diffusion and preserving interface sharpness. The surface tension source term F_σ is modeled using the Continuum Surface Force (CSF) model proposed by Brackbill et al. [30]:

$$F_\sigma = \sigma \frac{\rho k_l \nabla \alpha_l}{\frac{1}{2}(\rho_l + \rho_g)} \tag{6}$$

where σ is the surface tension coefficient, and k_l is the interface curvature defined from the gradient of the liquid volume fraction as $k_l = \nabla \cdot (\frac{\nabla \alpha_l}{|\nabla \alpha_l|})$.

2.4. Discrete Phase Model and VOF-to-DPM Transition Mechanism

The DPM tracks the trajectories of discrete droplets, bubbles, or solid particles in a Lagrangian reference frame. The equation of motion is derived from Newton's second law:

$$\frac{du_p}{dt} = F \tag{7}$$

where u_p is the particle velocity, and F represents the total force per unit particle mass, which may include contributions from aerodynamic drag, gravity, buoyancy, virtual mass, pressure gradient, and other forces. For the gas–liquid atomization conditions of this study, aerodynamic drag is the dominant interphase force and is expressed as

$$\mathrm{F_D} = \frac{18\mu}{\rho_p d_p^2} \frac{\mathrm{C_D Re_p}}{24} (\mathrm{u} - \mathrm{u_p}) \tag{8}$$

where d_p is the particle diameter, Re_p is the particle Reynolds number, and C_D is the drag coefficient. To account for significant droplet deformation under aerodynamic forces, the Dynamic Drag Model is adopted. This model computes the droplet distortion parameter, y, using the Taylor Analogy Breakup (TAB) model, and linearly adjusts the drag coefficient between that for a sphere $(y = 0)$ and that for a disk $(y = 1)$.

A key innovation of this study is the automatic VOF-to-DPM transition mechanism. During the computation, the solver scans the VOF field at regular intervals to identify isolated liquid blobs that have detached from the continuous liquid core. A liquid blob is converted into a DPM parcel only if it simultaneously satisfies two criteria. The first is a size criterion: the volume-equivalent spherical diameter of the blob must not exceed 0.4 mm. The second is a shape criterion: the asphericity of the blob, quantified by the standard deviation of surface distances from the centre of mass, must be below 0.5. This mechanism is triggered every five flow time steps. Only blobs meeting both conditions are removed from the VOF domain and injected as Lagrangian parcels, with mass and momentum conserved in the transition.

3. Numerical Simulation Overview

3.1. Research Object and Computational Domain

The present study focuses on a gas–liquid two-phase coaxial impinging jet nozzle specifically designed for spray cooling applications. To perform numerical simulations while balancing computational accuracy and resource efficiency, a three-dimensional geometric model of the key flow regions of the nozzle was constructed. To simplify the model and reduce computational cost, secondary features such as chamfers and threads, which have only a minor influence on the flow field, were omitted. The effective fluid domain, including the central liquid channel, the annular gas channel, the nozzle exit face, and the external spray field, was extracted, as shown in Figure 1a. It mainly consists of a central liquid channel, a coaxial outer annular gas channel, and a replaceable impingement wall located directly below the outlet.

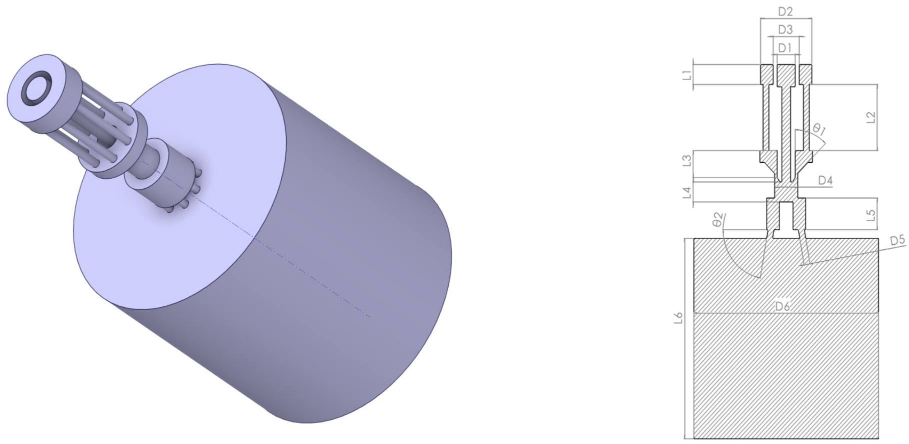

(**a**) Nozzle model (**b**) Dimensions marked on the X–Y plane

Figure 1. Nozzle model and X–Y cross-sectional figure.

The working principle of the nozzle is as follows. The nozzle delivers a central low-speed water jet and an outer annular high-speed air stream; the coaxial jets merge, impinge on the wall below, and spread radially into a thin liquid film. The main geometric dimensions of the nozzle are systematically summarized in Table 1, and the symbols are elaborately marked in Figure 1b. These parameters directly determine the flow areas and the interaction pattern of the gas–liquid two-phase flow and are critical structural variables influencing the atomization characteristics.

Table 1. Nozzle Geometric Parameters.

Symbols	Structural Parameters	Value
D1	Water inlet diameter	9.8 mm
L1	Flow conditioning section length	10.0 mm
D2	Air inlet outer diameter	27.6 mm
D3	Air inlet inner diameter	14.2 mm
L2	Flow development section length	33.0 mm
L3	Annular gap length	15.5 mm
$\theta 1$	Circular gap taper	45°
L4	Mixing chamber length	10.0 mm
D4	Mixing chamber diameter	12.5 mm
L5	Diffuser section length	16.0 mm
$\theta 2$	Outlet wall inclination	80°
D5	Outlet diameter	3.2 mm
D6	External domain diameter	100.0 mm
L6	External domain length	100.0 mm

3.2. Grid Independence Verification

A high-quality mesh is essential for ensuring the accuracy and convergence of CFD simulations. The nozzle configuration investigated in this study is characterized by a central tube and an annular gap with relatively small dimensions, whereas the external spray field occupies a large spatial scale. To accommodate such drastic scale variations and to maintain adequate resolution in boundary layer regions, a block-structured hexahedral meshing strategy was adopted. As shown in Figure 2, the entire computational domain was decomposed into several sub-blocks, within each of which high-quality hexahedral elements were generated using sweep or cooperative algorithms.

The Body of Influence (BOI) method was applied to concentrate local mesh refinement in regions with steep flow gradients, specifically the near-wall boundary layers inside the liquid orifice and annular gas gap, the gas–liquid mixing shear layer where the two jets converge at the nozzle exit to capture early instability development, and the impingement core zone covering the wall and the anticipated liquid film spreading area to resolve film morphology and breakup accurately.

Since the phase interface is tracked in the Eulerian framework before the liquid hits the impingement wall, the initial mesh must be fine enough to resolve the interface accurately. To check the influence of mesh resolution, four successively refined meshes were generated with approximately 0.9, 1.4, 1.9, and 2.4 million cells, all using identical boundary conditions, physical models, and numerical schemes. Axial liquid velocity along the flow path—from the inlet through the forming and developing sections to the mixing chamber—was used as the evaluation criterion. As shown in Figure 3, the 0.9 and 1.4 million cell meshes failed to reproduce the flow field accurately, whereas the velocity profiles from the 1.9 and 2.4 million cell meshes were essentially identical. Balancing accuracy and computational cost, the 1.9 million cell mesh was selected for all subsequent operating condition simulations.

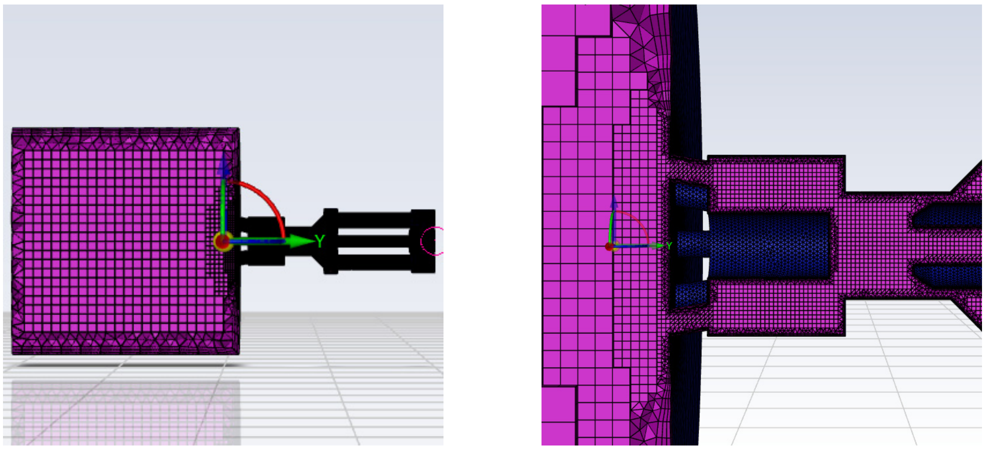

(**a**) Computational domain grid

(**b**) Partial enlarged detail

Figure 2. Schematic diagram of structured grid and near-wall region.

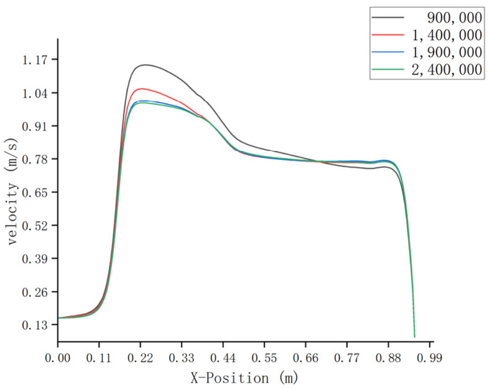

Figure 3. Grid independence verification.

3.3. Application of Grid Adaptation

The atomization process is intrinsically characterized by the drastic and complex temporal evolution of the gas–liquid interface topology, encompassing liquid film spreading, thinning, and perforation, as well as ligament stretching and breakup. A fixed initial mesh, regardless of its level of refinement, is generally incapable of providing sufficient resolution at every location and time instant. For this reason, AMR was activated throughout the entire transient simulation in the present study.

As shown in Figure 4, the core idea of AMR is to dynamically densify the mesh in regions with high gradient changes based on the gradient variations in flow field variables, and to coarsen and restore the mesh in regions with gentle gradients or where the interface is far away. The actual effect of AMR in this study is shown in Figure 5a,b, reflecting how the mesh adapts to the liquid-phase volume fraction over a certain period. In this study, the final number of grids reached 7.1 million. The gradient of the liquid-phase volume fraction was chosen as the refinement criterion, and the specific settings are as follows:

1. Refinement criterion: A computational cell was tagged for refinement when the calculated gradient of the liquid volume fraction exceeded 0.005.
2. Coarsening criterion: A cell was tagged for coarsening when the corresponding gradient fell below 0.001.
3. Maximum refinement level: This was set to 4, which permitted an initial hexahedral cell to be subdivided into a maximum of 4096 child cells.
4. Adaptation frequency: To strike a balance between computational overhead and accuracy, the mesh adaptation procedure was executed every two time steps.

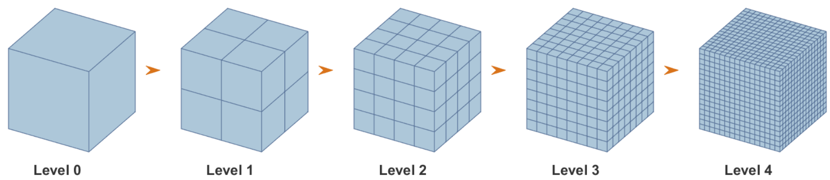

Figure 4. Illustration of the grid refinement process.

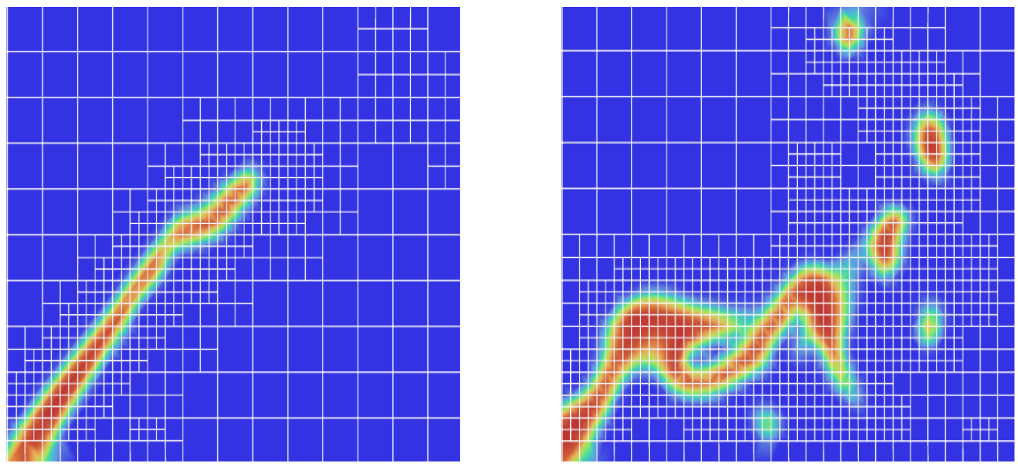

(**a**) The grid at the initial moment (**b**) The grid after the AMR

Figure 5. The process of adaptively partitioning the grid according to the gradient of liquid-phase volume fraction.

3.4. Parameter Setting

The numerical model was configured with a pressure-based transient solver and the SST $k-\omega$ turbulence model. The multiphase treatment employed an explicit VOF scheme with sharp interface modeling, coupled to the DPM framework through the size and shape criteria listed in Table 2.

Table 2. Basic simulation parameters.

Type	Parameters	Value
Solver	Solver type Gradient discretization scheme Pressure discretization scheme	Pressure-based, transient Least squares cell-based PRESTO!
Turbulence	Turbulence model Wall function	$SST\ k-\omega$ No-slip, adiabatic, standard roughness
Multiphase model	VOF scheme Surface tension model	Explicit, Sharp Interface Modeling CSF
Discrete phase	Secondary breakup model Sub-models	TAB Stochastic collision, coalescence
VOF-to-DPM	Size criterion Shape criterion Conversion frequency Parcel treatment	400 µm 0.5 Every 5 flow time steps Mass and momentum conserved per event
AMR	Mesh refinement frequency Minimum cell size Maximum refinement level	Every 2 time steps 5 µm 4
Time progression method	Time stepping method Global Courant number	Adaptive 1

4. Experimental Verification

4.1. Droplet Size Measurement

A spray visualization test rig was constructed for the gas–liquid two-phase impinging spray, as shown in Figure 6. The platform employed two non-contact optical instruments: a high-speed camera for spray morphology and a Malvern Spraytec laser diffraction analyzer for droplet sizing. Observation windows with quartz glass were installed on the pipe to permit optical access.

Figure 7 displays the Malvern Spraytec system and its on-site arrangement. The droplet size distribution was measured using a Malvern Spraytec laser diffraction system (Malvern Instruments, Malvern, Worcestershire, UK). The instrument consists of a transmitter module, a receiver module, and an optical mounting rail. The transmitter houses a 635 nm helium–neon laser and a 300 mm focal length lens. The laser beam is scattered by the spray droplets passing through the measurement zone, and the scattered light is collected by 36 detectors arranged in a concentric ring array within the receiver. Detector 0, located at the centre of the receiver, captures the unscattered beam; a higher signal at this detector corresponds to lower obscuration. Detectors 1 through 35 are positioned at increasing radial distances, with the detector index inversely related to the detectable particle diameter. After background light intensity correction, the detector signals are processed by the Spraytec software to compute the particle size distribution.

The transmitter and receiver are mounted at opposite ends of the optical rail, which ensures lens alignment and incorporates signal transmission cables. The inter-module distance can be adjusted as required. In the present study, the system was operated at a sampling frequency of 10 kHz with a measurement zone diameter of 18 mm, covering a size range of 0.05 to 2000 µm. Data acquisition was triggered automatically when the obscuration reached 70%. For each measurement, the Sauter mean diameter was calculated from 100 consecutive sample points taken from the central stable region of the time series.

Each operating condition was measured ten times. For more detailed information about the instrument and its usage methods, please refer to Reference [31].

The Malvern laser diffraction particle size analyzer was used to measure the droplet size distribution of the cooling water spray. The particle size distribution is shown in Figure 8. The horizontal axis represents the droplet diameter. The histogram, corresponding to the right vertical axis, displays the frequency of each size class, with higher frequencies indicating larger proportions of droplets of that size. The red curve, corresponding to the left vertical axis, represents the cumulative volume fraction. Rising from 0% to 100%, this curve indicates the cumulative percentage of all droplets smaller than a given diameter. The SMD value was directly obtained from the particle size analysis report generated by the Malvern system.

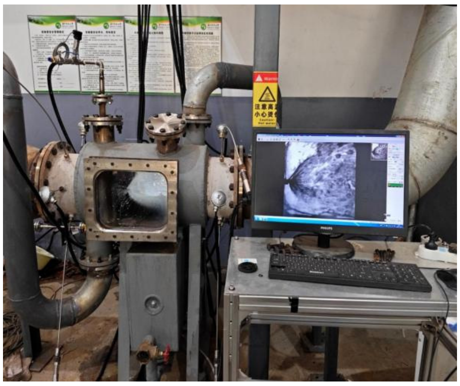

Figure 6. Spray Visualization Experimental Platform.

(**a**) Malvern laser particle size analyzer

(**b**) Arrangement of the particle size analyzer on the test bench

Figure 7. Droplet Diameter Measurement Test Bench.

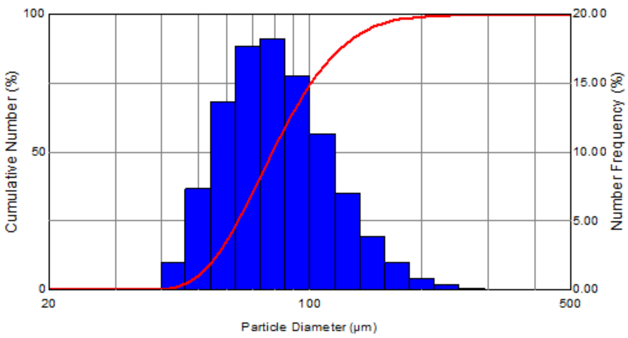

Figure 8. Particle size distribution frequency graph.

4.2. Spray Cone Angle Measurement

Figure 9a shows the high-speed camera arrangement. The optical system comprises a high-frequency pulsed LED light source, a Fresnel lens, a 532 nm bandpass filter, and a high-speed camera. The LED source emits pulsed light synchronised with the camera trigger signal at half the camera frame rate. The 532 nm bandpass filter, matched to the central wavelength of the LED, suppresses ambient light and ensures that the camera receives only the illumination signal, thereby reducing systematic errors.

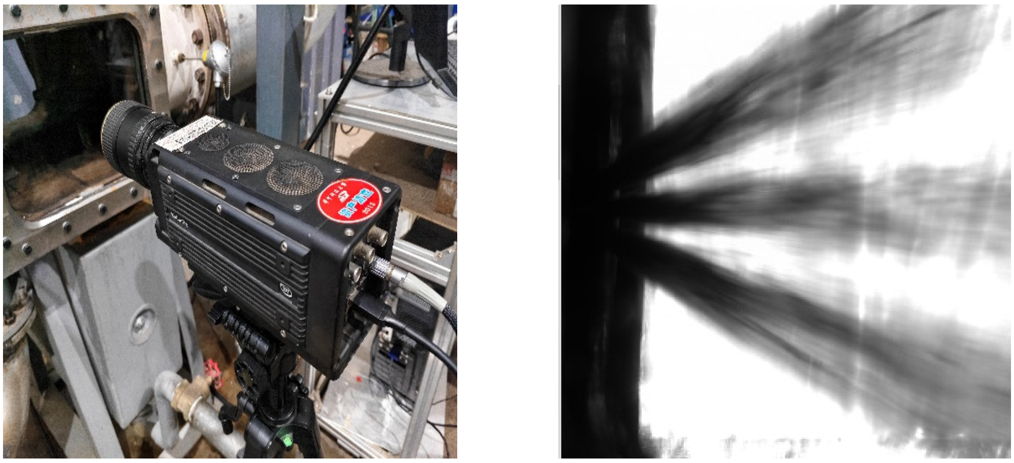

(**a**) Arrangement of high-speed cameras (**b**) Camera view window

Figure 9. Spray cone angle testing bench.

The camera employed is a Motion Pro Y4-S1 high-speed CMOS camera, operated at 20,000 frames per second with an exposure time of 3.3 µs. The LED source was placed on one side of the spray and the camera on the opposite side, with the camera mounted on a tripod and positioned such that the entire spray development region fell within the field of view. The white light emitted by the LED passed through a Fresnel lens, which scatters the beam into a uniform parallel illumination field covering the measurement window. The Fresnel lens used here is a multi-ring equal-thickness convex lens, thinner than a conventional convex lens because only the curved optical surface is retained. The cooling nozzle is located at the left centre of the image plane. As illustrated in Figure 9b, the backlighting method was adopted for spray visualization: as the water spray develops, droplets scatter and absorb the incident light, appearing as dark regions against the bright background, which enables clear identification of the spray morphology. The pulse frequency and pulse width of the LED were 10,000 Hz and 3.33 µs, respectively. For more information about the imaging system and its usage methods, please refer to Reference [32].

Because the cooling water spray in a high-speed gas flow suffers from strong background interference, an in-house Python code was developed for post-processing the high-speed camera images. This improved the measurement accuracy and allowed the macroscopic spray parameters to be derived from the images.

Figure 10 shows the image processing workflow. Starting from the raw spray image on the left, a background image was first subtracted to remove background noise. Based on the intensity contrast in the background-removed image, a boundary threshold was automatically determined. The image was then converted to a binary image, and the spray contour was extracted using a connected-component analysis. According to the low-pressure spray theory, nearly straight non-atomized regions on the upper boundary of the spray were identified, as indicated by the blue curves in the second panel. Finally, the points on these blue curves were fitted with straight lines by the least-squares method, and the angle between the two fitted lines was taken as the spray cone angle. All the experiments were conducted at room temperature (approximately 25 °C) and under normal pressure. And the same algorithm was applied in all cases.

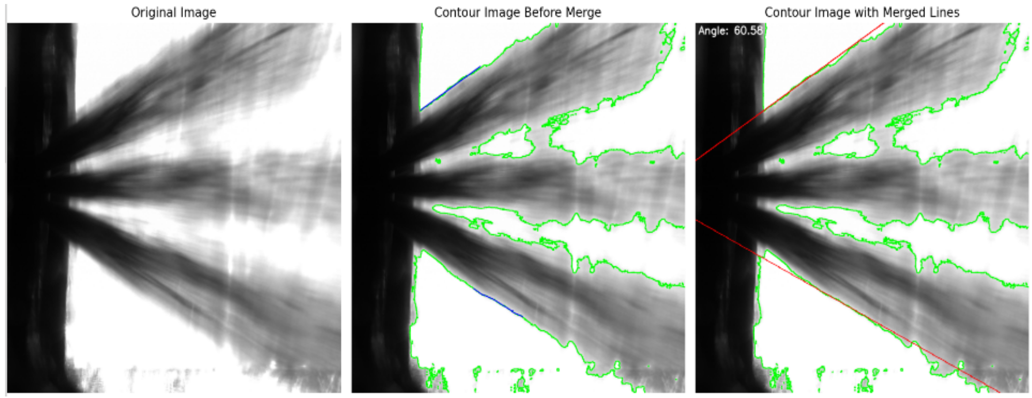

Figure 10. Processing procedure of the spray images.

5. Results and Discussion

5.1. Validation of Numerical Model Against Experimental Data

A quantitative comparison between simulation and experiment was essential to establish confidence in the VOF-DPM framework. Four representative operating conditions were examined, spanning high-, low-, and medium-pressure zones. In the high-pressure zone, both the inlet pressure and the water inlet pressure were set to 0.28 MPa. In the low-pressure zone, these two inlet pressures were maintained at 0.12 MPa. The medium-pressure zone included two distinct conditions: one with an inlet pressure of 0.20 MPa and a water inlet pressure of 0.16 MPa, and the other with an inlet pressure of 0.16 MPa and a water inlet pressure of 0.20 MPa. Verification points were selected from different pressure zones, making the test both rigorous and economical in assessing the numerical model's predictive accuracy. The model employed the same boundary conditions and geometric parameters as the experiment, allowing a direct comparison to validate the numerical model. The comparison focused on two primary macroscopic atomization characteristics: the spray cone angle and the droplet size distribution.

Figure 11 presents parity plots comparing the numerically predicted and experimentally measured spray cone angle and SMD across the four validated conditions, which together span the full operating envelope of the study. In a parity plot, perfect agreement between simulation and experiment corresponds to all data points falling on the "y = x" reference line; the deviation envelope provides a visual benchmark for engineering acceptability. For the spray cone angle, all four points lie within ±2% of the parity line, with the maximum relative error being 1.81%. The points are distributed on both sides of reference line, indicating the absence of a systematic over- or under-prediction bias. For the SMD, the relative errors range from 2.67% to 5.59%, with all data points inside the ±6% band. The horizontal error bars represent experimental measurement uncertainty and are conceptually distinct from the vertical displacement of each data point from the parity line, which quantifies the simulation–experiment deviation. The close clustering of all validation points near reference line, supports the conclusion that the coupled VOF–DPM framework provides quantitatively reliable predictions throughout the operating range considered in this study, thereby justifying its use for the subsequent pressure ratio optimization and nozzle redesign analyses.

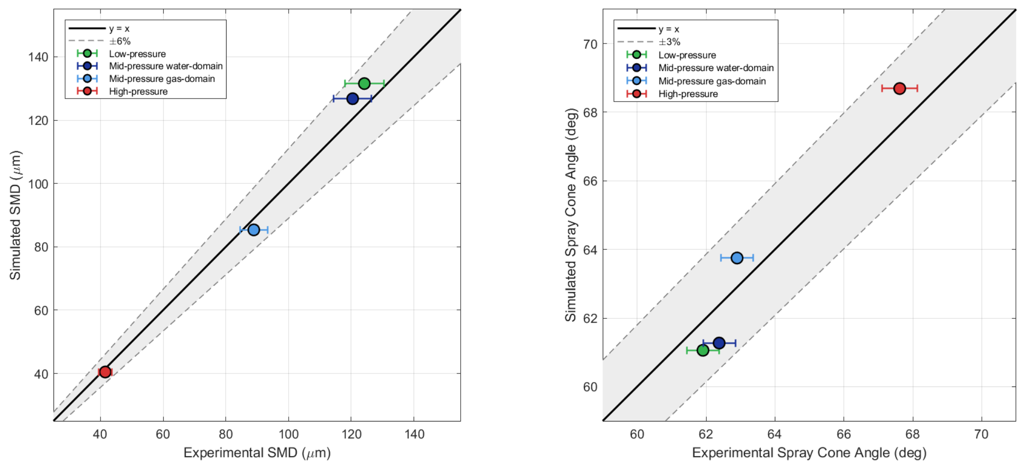

(**a**) Sauter Mean Diameter (**b**) Spray Cone Angle

Figure 11. Parity plot comparing experiments and numerical models under typical operating conditions.

5.2. *Spray Morphology and Breakup Process*

Figure 12 shows the particle trajectories of a gas–liquid coaxial impinging-wall atomization nozzle over a period from 0 to 400 μs. The green isosurface represents the water volume fraction of 0.5, commonly regarded as the gas–liquid interface. The colored dots indicate Lagrangian droplets converted from the continuous phase through the VOF-to-DPM transition mechanism. The droplet sizes are scaled down in the figure for clarity, and the actual sizes are distinguished by color.

Strong gas–liquid interaction persists throughout the computational domain, and the full primary and secondary breakup from continuous to discrete phase is captured. At 50 μs, the liquid appears as a smooth, intact film at the flow-conditioning exit; the high-speed gas has barely exchanged momentum with it, and no visible deformation or stripping occurs. From 100 to 150 μs, the gas intrudes in the streamwise direction, establishing a sharp tangential velocity gradient that triggers Kelvin–Helmholtz instability. Aerodynamic shear progressively overcomes viscous and surface tension forces, stretching and thinning the film edges, while slight interfacial disturbances signal the transition toward an unstable, breakup-prone state.

The 200–250 μs interval is dominated by primary breakup: intensified momentum exchange and a normal velocity gradient drive Rayleigh–Taylor instability. These combined instabilities violently tear the thinned film, stripping annular sheets, slender ligaments, and large liquid lumps from the main body. Ligaments, ribbon-like fragments, and large droplets constitute the typical structures of this stage. Between 300 and 350 μs, the ligaments and large droplets generated by primary breakup undergo secondary breakup under sustained gas shear and impact. Interfacial disturbances fragment the ligaments, and large droplets further disintegrate through the coupled effects of aerodynamic and inertial forces; the number of small droplets rises rapidly, the size distribution continuously refines, gas–liquid mixing intensifies, and the morphology shifts quickly from large lumps to fine droplets. By 400 μs, both breakup stages are essentially complete: ligaments and lumps have fully broken into discrete fine droplets, interfacial disturbances are subdued, the droplet size distribution becomes more uniform, and the atomization pattern reaches a comparatively steady, efficient state. Figure 13 presents the VOF-tracked evolution of the liquid volume fraction.

These instabilities govern the primary breakup, but the final droplet size is determined by a broader competition among several forces. Aerodynamic inertia, represented by the gas-phase Weber number, acts to stretch and tear the liquid structures. Surface tension acts as a restoring force that resists deformation and promotes the return to a spherical shape. Viscous stresses within the liquid dissipate kinetic energy and reduce ligament thinning. Capillary pressure gradients along curved interfaces drive flow from thinner to thicker regions, accelerating necking and pinch off. This multiscale force balance, rather than any single instability, controls whether a ligament fragments into fine droplets or survives as a larger blob. Agnihotri et al. [33] reviewed droplet breakup across diverse flow configurations and concluded that the outcome is universally determined by the local balance of inertial, capillary, and viscous forces, regardless of the specific breakup geometry.

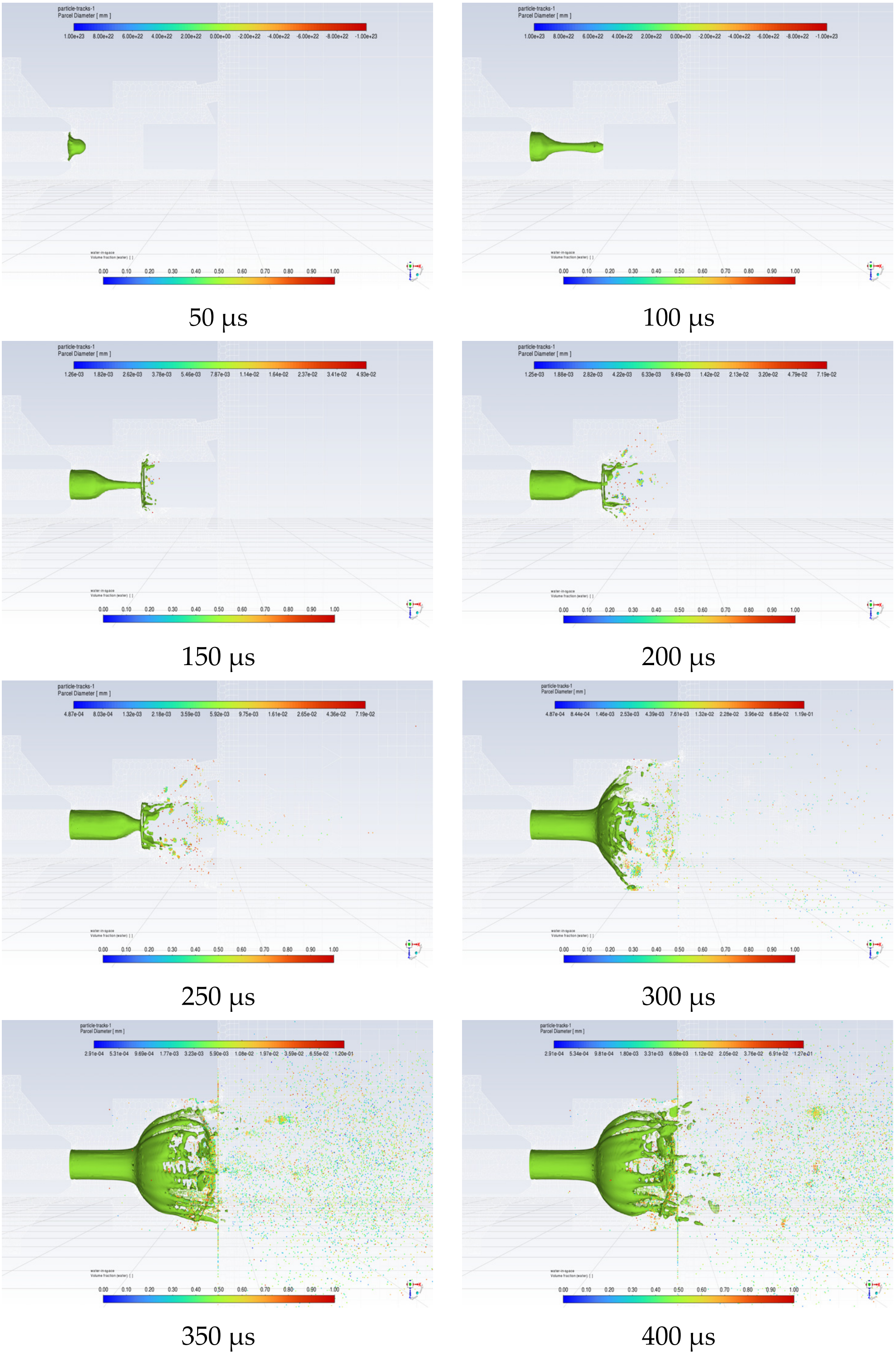

Figure 12. Breakup process of the liquid film.

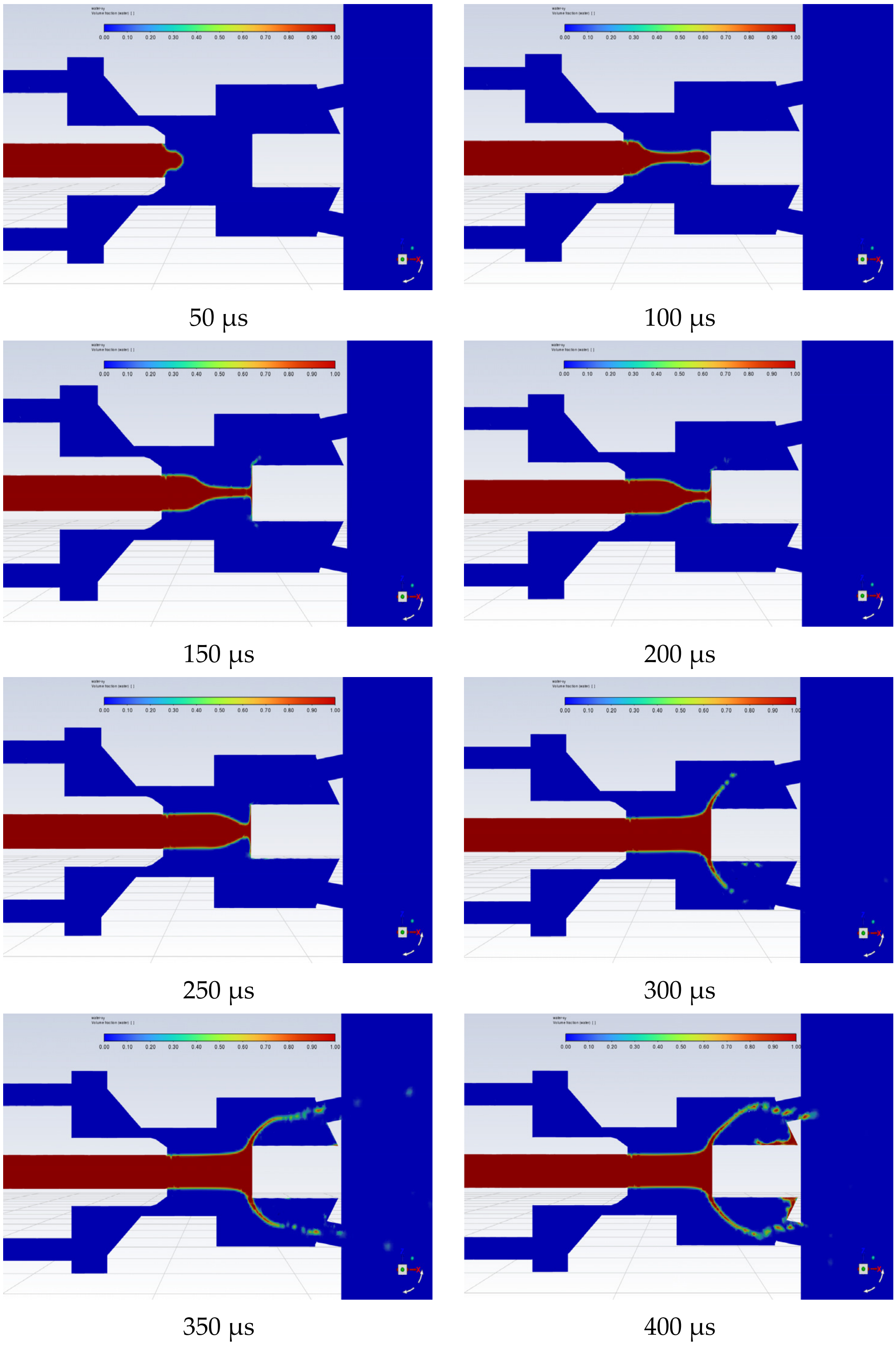

Figure 13. Change in liquid-phase volume fraction.

5.3. Effect of Air Inlet Pressure on Spray Cone Angle and SMD

Figure 14 maps the SMD and spray cone angle variations with air inlet pressure under five fixed water inlet pressures to illustrate how air inlet pressure regulates atomization characteristics. The SMD decreased monotonically with increasing air inlet pressure under all water inlet pressure conditions. For a water inlet pressure of 0.28 MPa, raising the air inlet pressure from 0.12 MPa to 0.28 MPa drove the SMD from 149.04 µm down to 40.46 µm—a 72.85% drop. This behavior is consistent with Kelvin–Helmholtz instability at the gas–liquid interface: the tangential velocity gradient between the high-speed annular airflow and the low-speed central liquid jet creates an intense shear layer that drives the growth and breakup of surface waves on the liquid film. Higher air inlet pressure increases the momentum flux in that shear layer, destabilizing the liquid film earlier and yielding finer droplets.

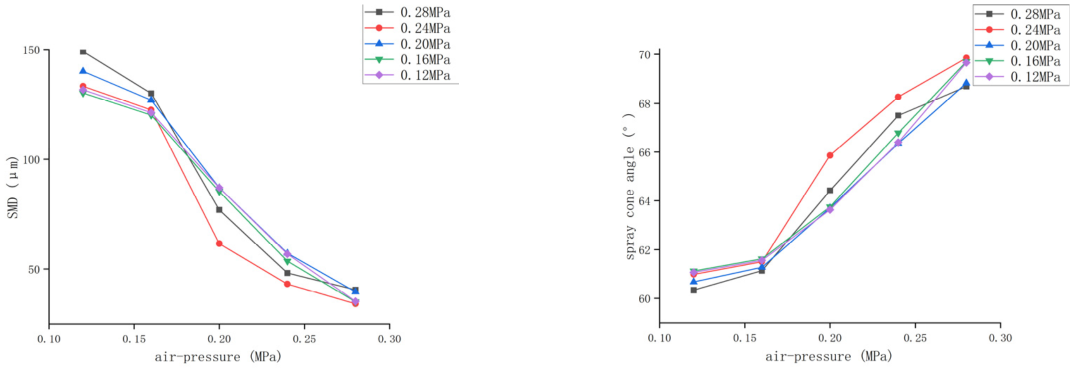

(**a**) SMD variation with respect to inlet air pressure (**b**) Spray cone angle variation with respect to inlet air pressure

Figure 14. The effect of inlet air pressure on the atomization characteristics.

The spray cone angle also increased with air inlet pressure, but the variation was much smaller than that of SMD. For a water inlet pressure of 0.20 MPa, when the air inlet pressure was raised from 0.12 MPa to 0.28 MPa, the cone angle widened from 60.67° to 68.83°, an increase of only about 13.4%. This limited sensitivity resembles the "pressure-insensitive cone angle" phenomenon reported by Krištof et al. [34] for spiral nozzles, though the underlying reason differs. In the present configuration, the cone angle is primarily governed by the geometric constraint of the impingement wall; higher air inlet pressure mainly strengthens radial spreading without dramatically altering the macroscopic spray envelope. From an engineering standpoint, this feature is desirable—one can adjust SMD over a wide pressure range without worrying that the cone angle will stray outside the required cooling coverage.

It was also observed that as air inlet pressure increased, the SMD reduction rate and the cone angle increase rate both slowed. To quantify this diminishing effect, the per-unit-pressure SMD sensitivity was computed in three consecutive segments at a fixed water inlet pressure of 0.28 MPa. In the 0.20–0.24 MPa range, the sensitivity was approximately 7.2 μm per 0.01 MPa. In the 0.24–0.28 MPa range, it dropped to 1.9 μm per 0.01 MPa. Raising the air inlet pressure from 0.28 to 0.30 MPa further reduced the sensitivity to 1.4 μm per 0.01 MPa. The sequential decline from 7.2 to 1.9 to 1.4 μm per 0.01 MPa matches the experimental observation that atomization improvements weaken as air inlet pressure increases, confirming that the VOF–DPM reproduces the correct trend.

5.4. Effect of Water Inlet Pressure on Spray Cone Angle and SMD

Figure 15 shows how SMD and spray cone angle vary with water inlet pressure under five constant air inlet pressures. The water inlet pressure effect stands in stark contrast to the monotonic behavior of air inlet pressure—it displayed a clear region-dependent trend. In the higher water inlet pressure region, SMD first decreased and then increased as water inlet pressure rose. When the water inlet pressure was raised from 0.12 MPa to 0.28 MPa, a minimum SMD emerged at 0.24 MPa, indicating a transition in the underlying physical competition. At low water inlet pressure, insufficient liquid supply led to uneven film spreading on the impingement surface and local dry spots that degraded atomization quality. As water inlet pressure increased, the liquid film became more uniform, and atomization improved. Beyond a certain point, however, the film inertia grew too large, increasing its resistance to aerodynamic breakup and causing the SMD to rise again.

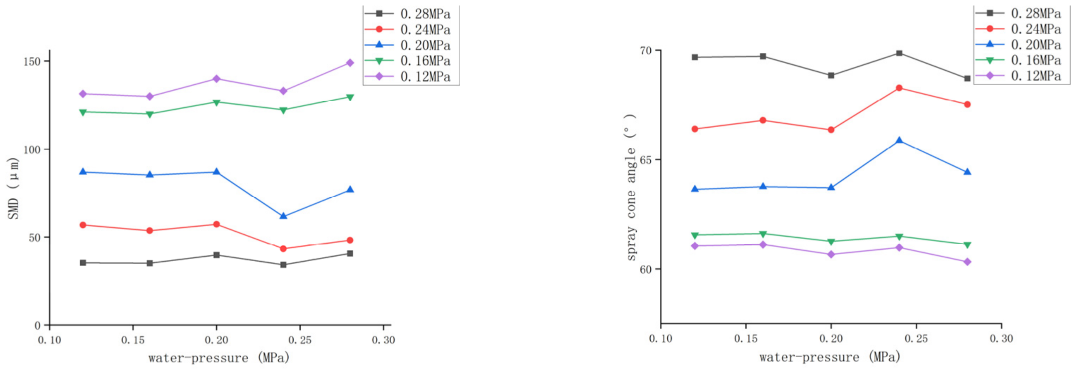

(**a**) SMD variation with respect to inlet water pressure (**b**) Spray cone angle variation with respect to inlet water pressure

Figure 15. The effect of inlet water pressure on the atomization characteristics.

A second single-variable test was conducted to examine the nonlinear influence of water inlet pressure. With the air inlet pressure fixed at 0.28 MPa, raising the water inlet pressure from 0.28 to 0.30 MPa caused the SMD to increase by 5.2 percent and the cone angle to decrease by 1.9 percent. The direction of these changes is opposite to that produced by increasing the air inlet pressure. Raising the water inlet pressure at an already high operating level thus degrades atomization quality. This behaviour is consistent with the experimental finding that water inlet pressure exerts a nonmonotonic influence on spray characteristics. The ability of the model to capture this sign reversal using the same VOF–DPM framework provides strong evidence that the competition between aerodynamic shear and liquid inertia at the impingement point is adequately resolved by the simulation.

This nonlinear response arises from the force balance discussed above. At moderate water inlet pressures, the thin film is dominated by aerodynamic shear. As the water inlet pressure increases, the film thickens and its inertia grows, increasing the characteristic length scale of the Kelvin–Helmholtz instability and shifting the most unstable wavelength to larger values. The higher liquid momentum also raises the Weber number threshold for aerodynamic stripping. At sufficiently high water inlet pressures, the film inertia overwhelms the available aerodynamic force and atomization quality degrades. This transition from a shear dominated to an inertia limited regime is conceptually similar to the viscous to inertial breakup transition observed by Ma et al. [35] for droplets in confined geometries, where the balance between driving and resisting forces determines whether fragmentation occurs.

It should be noted that the atomization metrics reported in this study, namely SMD and spray cone angle, are cold flow indicators of spray quality. They are directly relevant to cooling performance because they control droplet impingement density, surface coverage, and film morphology on the hot wall. However, the translation from improved atomization to improved cooling effectiveness requires further validation that includes heat transfer, phase change, and temperature dependent fluid properties. The optimization strategies proposed here should therefore be regarded as atomization level guidance whose thermal performance implications await future experimental confirmation under high temperature conditions.

5.5. Multi-Objective Matching and Optimization of Gas–Liquid Pressure Based on Total Drive Power Constraint

The analyses in Sections 5.3 and 5.4 reveal two key findings: air inlet pressure is the dominant variable controlling SMD, but the "higher is better" monotonic trend breaks down in the high water inlet pressure region; and the effect of water inlet pressure on SMD is non-monotonic in the low air inlet pressure region, indicating the existence of an optimal matching point. This gives rise to a practically important question: under the limited power budget of a marine power station, how should the driving power be distributed between the compressor and the pump to achieve the best atomization performance?

The design space is modest and the 25-point dataset is sufficient only for a low order fit. A quadratic surrogate was therefore adopted to capture the gross SMD trend, and the genetic algorithm was used simply as a constrained search tool. The problem is not a trivial boundary optimum because air inlet pressure dominates atomization yet costs far more power per unit pressure than water. Under a fixed total power budget the two pressures cannot be maximised simultaneously, so a search algorithm is needed to locate the trade-off. The result is a feasibility demonstration of the pressure ratio design concept, not a production ready control law.

For a fixed-geometry nozzle and assuming incompressible orifice flow, the volumetric flow rate is proportional to the square root of the pressure drop. The total hydraulic driving power can be expressed accordingly:

$$\mathrm{W_{total}} = \mathrm{P_aQ_a} + \mathrm{P_wQ_w} = \alpha \mathrm{P_a^{3/2}} + \beta \mathrm{P_w^{3/2}} \tag{9}$$

Here, $\alpha = C_{d,a}A_a\sqrt{2/\rho_a}$, $\beta = C_{d,w}A_w\sqrt{2/\rho_w}$. For the present nozzle, $Aa/Aw \approx 5.83$, $\rho_w/\rho_a \approx 8.3 \times 10^2$, $\alpha/\beta \approx 1.7 \times 10^2$, the power cost required to generate a unit water inlet pressure is far lower than that for a unit air inlet pressure. To simplify the optimization while maintaining physical transparency, a dimensionless total equivalent pressure coefficient is introduced:

$$\Pi(\mathrm{P_a}, \mathrm{P_w}) = \mathrm{P_a} + \eta \mathrm{P_w} \tag{10}$$

where the weighting factor η reflects the efficiency ratio and flow area ratio between the compressor and the pump. A baseline value of $\eta = 0.5$ is adopted in this study. The constrained optimization problem is formulated as: minimize SMD, subject to $\mathrm{P_a} + 0.5\mathrm{P_w} \leq \Pi_{\mathrm{max}}$; $0.12 \leq \mathrm{P_a}, \mathrm{P_w} \leq 0.30$ MPa. A quadratic polynomial surrogate model is constructed based on 25 orthogonal simulation data points. A genetic algorithm is used to solve the optimization:

$$\widehat{\mathrm{SMD}}(\mathrm{P_a}, \mathrm{P_w}) = c_0 + c_1\mathrm{P_a} + c_2\mathrm{P_w} + c_3\mathrm{P_a^2} + c_4\mathrm{P_w^2} + c_5\mathrm{P_aP_w} \tag{11}$$

Figure 16 shows the SMD response surface and the GA-identified optimal solutions under different constraint levels.

1. Unconstrained optimum ($\Pi_{\mathrm{max}} = 0.6$ MPa): GA converges to Pa = 0.28, Pw = 0.24 MPa, yielding SMD = 34.12 μm. This exactly corresponds to the non-monotonic minimum found in Section 5.3, demonstrating that even under "full power" conditions, the optimum does not simply correspond to the maximum of both pressures but to a specific pressure ratio.
2. Moderate constraint ($\Pi_{\mathrm{max}} = 0.45$ MPa): The optimal solution is approximately Pa $\approx$ 0.28 MPa, Pw $\approx$ 0.16 MPa, with a pressure ratio of about 1.75. This indicates that when power is limited, priority should be given to air inlet pressure to maintain the shear breakup capability.

3. Tight constraint ($\Pi_{max} = 0.35$ MPa): The feasible region shrinks significantly, and the optimal point lies near the upper bound of Pa and the lower bound of Pw, further confirming the physical fact that air inlet pressure dominates atomization.

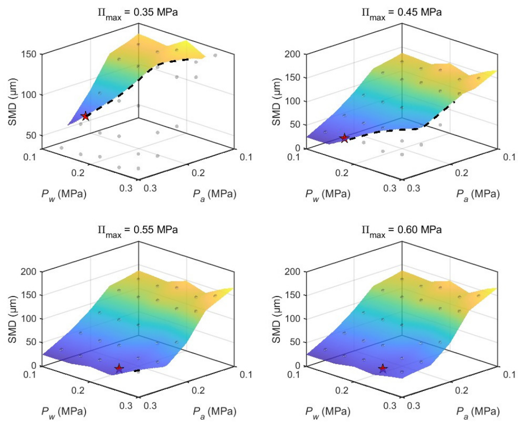

Figure 16. SMD response surface and GA optimal solution position.

When the power allocated to the spray system from a marine power station is limited, an asymmetric "high air inlet pressure and low water inlet pressure" strategy is recommended. For a total pressure budget of Pi = 0.45 MPa, setting Pa = 0.28 MPa and Pw = 0.16 MPa achieves the optimum under the constraint and improves atomization fineness by approximately 59% compared with an equal-pressure distribution scheme.

5.6. Optimization of Nozzle Structure

Due to the limited import pressure, it is not possible to simply enhance the atomization effect through pressure increase experiments. Therefore, the optimization of the nozzle structure becomes particularly important. Numerical simulations revealed that the original horizontal impingement surface of the nozzle tended to cause coalescence of droplets from primary breakup inside the mixing chamber. To significantly improve atomization, this study proposes replacing the original horizontal surface with a full-cone impingement surface.

Figure 17 shows the velocity cloud diagrams of the cross-sections beneath two impingement surfaces at a certain moment, while Table 3 presents the SMD and cone angle values before and after the structural optimization.

The difference in data arises because the full-cone impingement surface imparts a stronger surface breakup capability to the continuous water jet and accelerates the droplets produced by primary breakup as they leave the mixing chamber. Furthermore, under the same conditions, the full-cone impingement surface generates a larger spray cone angle. This results from the fact that greater liquid momentum after impingement yields a higher initial axial spreading velocity. This modification is of considerable significance for cooling applications using gas–liquid coaxial impingement nozzles.

The underlying physical reason for this improvement relates to the geometry mediated redistribution of the liquid film. On a flat surface the impinging liquid spreads into a relatively thick, slow-moving film whose residence time on the surface is long. The thick film shields the interior from the high-speed gas, and only the outer periphery participates in aerodynamic stripping. The conical surface, by contrast, promotes rapid radial spreading and continuous thinning of the film as it travels outward along the inclined wall. This reduces the local film thickness, increases the surface-to-volume ratio exposed to the gas shear, and shortens the residence time before the film leaves the impingement region. The result is more efficient momentum transfer from the gas phase to the liquid phase per unit liquid mass. Gao et al. [36] demonstrated a similar principle in a microfluidic context, where geometric splitting of a droplet path controlled the breakup outcome by redistributing the local stress field. The present conical surface achieves an analogous effect at the macroscopic scale.

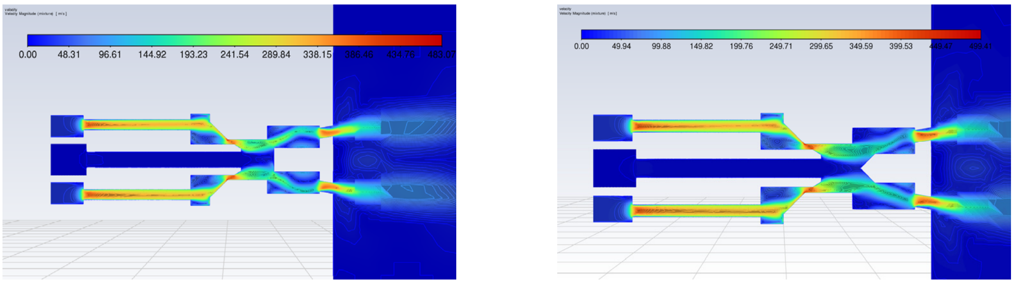

(**a**) Planar impingement surface (**b**) Full conical impingement surface

Figure 17. Velocity field comparison before and after structural optimization.

Table 3. Comparison of atomization characteristics before and after structural optimization.

Parameter	Planar Impingement Surface	Full Conical Impingement Surface	Improvement Rate
Spray Cone Angle	63.75°	66.08°	3.6%
Sauter Mean Diameter	85.34 μm	60.28 μm	29.36%

6. Conclusions

This study focuses on spray cooling applications. A multiscale coupled VOF–DPM combined with AMR was employed to conduct an in-depth numerical investigation of the atomization process in a gas–liquid coaxial impingement nozzle, with experimental validation. Based on the validated model, the influence of the gas–liquid pressure ratio on atomization characteristics was systematically examined. The main conclusions are summarized as follows:

1. By integrating the VOF method, the DPM method, and AMR, a high-fidelity three-dimensional transient CFD model was successfully established. Comparisons of the spray cone angle and SMD with experimental data verified the accuracy and reliability of the model. The model is capable of capturing key atomization subprocesses in detail, including liquid film spreading, destabilization, perforation, ligament stretching, and breakup.
2. At ambient pressure, 25 orthogonal experiments were conducted to measure SMD and the cone angle. The results revealed the nonlinear effects of air inlet pressure and water inlet pressure on atomization quality. At a constant water inlet pressure, the SMD decreased gradually with increasing air inlet pressure, but the reduction became less pronounced at high air inlet pressures. At a constant air inlet pressure, both the SMD and the cone angle exhibited local extrema as the water inlet pressure increased, indicating that the influence of water inlet pressure on atomization is nonlinear.
3. Under the condition that the air inlet pressure and water inlet pressure are limited by the total driving power, the constraint optimization for the pressure matching of air and water was carried out. Optimal power allocation strategies under different constraint levels were provided for a given ship power station capacity.
4. As a further exploration of structural design, the original planar impingement surface was compared with a full conical impingement surface under identical boundary conditions in the numerical model. The conical configuration predicted a 29.36-percent reduction in SMD, indicating that impingement surface geometry is a promising lever

for improving atomization quality. The underlying mechanism is attributed to the enhanced radial spreading and continuous film thinning along the inclined wall, which increases the surface-to-volume ratio exposed to the gas shear. This result identifies impingement geometry optimization as a worthwhile direction for future nozzle development.

Author Contributions: Conceptualization, J.Z.; methodology, R.W.; software, R.W.; validation, Q.W. and Z.W.; formal analysis, K.Y.; investigation, L.Z. and Y.Z.; resources, J.Z.; data curation, R.W.; writing—original draft preparation, R.W.; writing—review and editing, R.W., Z.W. and J.Z.; visualization, R.W.; supervision, R.W.; project administration, J.Z. All authors have read and agreed to the published version of the manuscript.

Funding: This research received no external funding.

Data Availability Statement: The data presented in this study are available on request from the corresponding author due to the data sharing policies of our affiliated institution.

Conflicts of Interest: The authors declare no conflicts of interest.

Abbreviations

The following abbreviations are used in this manuscript:

SMD	Sauter Mean Diameter
CFD	Computational Fluid Dynamics
VOF	Volume of Fluid
DPM	Discrete Phase Model
AMR	Adaptive Mesh Refinement
SST	Shear Stress Transport
CSF	Continuum Surface Force
TAB	Taylor Analogy Breakup
BOI	Body of Influence

References

1. Naganathan, A.; Holland, B.G.; Demirdogen, C.A. Simulation-Based Thermal Fatigue Validation Test Development for Exhaust Manifold. *J. Eng. Gas Turbines Power* **2024**, *146*, 081024. [CrossRef]
2. Okrajni, J.; Twardawa, M.; Wacławiak, K. Impact of Heat Transfer on Transient Stress Fields in Power Plant Boiler Components. *Energies* **2021**, *14*, 862. [CrossRef]
3. Peng, Y.; Niu, Z.; Zhu, S.; Qi, T.; Lv, C. Simulation Study on Temperature and Stress and Deformation on Encapsulated Surfaces under Spray Cooling. *Energies* **2024**, *17*, 1070. [CrossRef]
4. Cao, L.; Li, W.; Du, H. Aerodynamic performance and cooling effect of exhaust passage in steam turbine with new water spray scheme. *Heat Mass Transf.* **2024**, *60*, 1643–1665. [CrossRef]
5. Zhao, Y.; Gong, S.; Yang, Q.; Xuan, Z.; Li, W.; Xie, L.; Liu, L.; Ge, M. Experimental investigation of heat transfer performance in gas-atomized spray cooling. *Int. J. Heat Mass Transf.* **2024**, *218*, 124768.
6. Zhang, T.; Mo, Z.; Xu, X.; Liu, X.; Chen, H.; Han, Z.; Yan, Y.; Jin, Y. Advanced study of spray cooling: From theories to applications. *Energies* **2022**, *15*, 9219. [CrossRef]
7. Yang, X.; Shen, F.; Wang, J.; Wu, D.; Duan, L.; Duan, L.; Kang, Q. Numerical simulation of spray cooling heat transfer evolution based on experimental data. *Phys. Fluids* **2024**, *36*, 097109. [CrossRef]
8. Huang, X.Z.; Li, B.; Zhang, H.L.; Wang, W.W.; Zhao, F.Y.; Cai, Y. Optimizing spray cooling systems: A comprehensive study on influential parameters and their effects on heat transfer under varied heat flux conditions. *Numer. Heat Transf. Part A Appl.* **2025**, *86*, 2347–2371. [CrossRef]
9. Wan, H.; Liu, P.J.; He, G.Q.; Xue, Z.R.; Qin, F.; Li, W.Q. Experimental and numerical studies on the spray cooling of deionized water in non-boiling regime. *Case Stud. Therm. Eng.* **2023**, *44*, 102834. [CrossRef]
10. Poongavanam, G.; VinothKumar, S.; Vigneswaran, V.S.; Ramalingam, V.; Cheol, K.S.; Ramkumar, V. Spray cooling for hydrogen vehicle, electronic devices, solar and building (low temperature) applications: A state-of-art review. *Renew. Sustain. Energy Rev.* **2024**, *189*, 113931.
11. Mudawar, I. Recent advances in high-flux, two-phase thermal management. *J. Therm. Sci. Eng. Appl.* **2013**, *5*, 021012. [CrossRef]

12. Liang, L.; Jia, W.; Zhao, Q.; Zhang, L.; Zhou, Z.-F.; Chen, B. Spray and dynamic heat transfer induced by 2-methylfuran transient spray impingement on piston surface. *Int. J. Therm. Sci.* **2023**, *187*, 108154. [CrossRef]
13. Raveshi, M.R.; Keshavarz, A.; Mojarrad, M.S.; Amiri, S. Experimental investigation of pool boiling heat transfer enhancement of alumina–water–ethylene glycol nanofluids. *Exp. Therm. Fluid Sci.* **2013**, *44*, 805–814. [CrossRef]
14. Lee, S.J.; Kim, J.Y.; Lee, M.H.; Hong, J.G. Experimental study of twin-fluid flow differences and Sauter mean diameter prediction according to Y-jet nozzle mixing-tube design. *Int. J. Multiph. Flow* **2025**, *183*, 105063. [CrossRef]
15. Bar-Kohany, T.; Arogeti, M.; Malka, A.; Sher, E. Advances in Liquid Atomization via Flash Boiling—A Global Overview. *Energies* **2023**, *16*, 6763. [CrossRef]
16. Wang, B.; Wu, E.; Yang, A.; Zhang, F.; Yang, B.; Liu, Q.; Chen, X. Direct numerical simulations of high-pressure impinging-jet atomization: Interfacial evolutions and spray characteristics. *Chin. J. Aeronaut.* **2025**, *39*, 103778. [CrossRef]
17. Borisov, S.P.; Kudryavtsev, A.N. Development of the Rayleigh-Taylor instability. Results of numerical simulation at low Reynolds numbers. In *Proceedings of the AIP Conference Proceedings*; AIP Publishing LLC.: Melville, NY, USA, 2020; Volume 2288, p. 030019.
18. Yang, A.J.K.; Olsthoorn, J.; Timmermans, M.L. Sedimentation in particle-laden flows with and without velocity shear. *Phys. Fluids* **2023**, *35*, 086604. [CrossRef]
19. Zhang, R.; Li, Z.; Kang, J.; Chen, D.; Yuan, G.; Duan, F. Simulation on the spray cooling of a high-temperature cylindrical surface. *Int. J. Heat Mass Transf.* **2024**, *224*, 125334. [CrossRef]
20. Zhao, A.; Duwig, C.; Liu, C.; Gerada, D.; Leksell, M. Parameter study for oil spray cooling on endwindings of electric machines via Eulerian–Lagrangian simulation. *Appl. Therm. Eng.* **2023**, *235*, 121281. [CrossRef]
21. Luo, Z.; Liang, K.; Chen, X.; Li, Z.; Wang, X.; Zhou, H.; Wang, Y. Numerical investigation of the effect of vibration on spray cooling heat transfer in the non-boiling region. *Case Stud. Therm. Eng.* **2023**, *51*, 103518. [CrossRef]
22. Ghalambaz, S.; Abbaszadeh, M.; Sadrehaghighi, I.; Younis, O.; Ghalambaz, M.; Ghalambaz, M. A forty years scientometric investigation of artificial intelligence for fluid-flow and heat-transfer (AIFH) during 1982 and 2022. *Eng. Appl. Artif. Intell.* **2024**, *127*, 107334. [CrossRef]
23. Paladino, E.E.; Lima, J.A.; Pessoa, P.A.S.; Almeida, R.F. A computational model for the flow within rigid stator progressing cavity pumps. *J. Pet. Sci. Eng.* **2011**, *78*, 178–192. [CrossRef]
24. Wan, H.; He, G.Q.; Xue, Z.R.; Li, W.Q. Numerical study and experimental verification on spray cooling with nanoencapsulated phase-change material slurry (NPCMS). *Int. Commun. Heat Mass Transf.* **2021**, *123*, 105187. [CrossRef]
25. Adam, A.; He, W.; Fan, Y.; Han, D. Investigation of flow characteristics and mixing of liquid hydrogen within a premixing swirl tube for the turbine engine combustor. *Int. J. Hydrogen Energy* **2024**, *49*, 367–383. [CrossRef]
26. Eslami Majd, A.; Tchuenbou-Magaia, F.; Meless, A.M.; Adebayo, D.S.; Ekere, N.N. A review on cooling systems for portable energy storage units. *Energies* **2023**, *16*, 6525. [CrossRef]
27. Triplett, K.A.; Ghiaasiaan, S.M.; Abdel-Khalik, S.I.; Sadowski, D.L. Gas–liquid two-phase flow in microchannels Part I: Two-phase flow patterns. *Int. J. Multiph. Flow* **1999**, *25*, 377–394.
28. Pakhomov, M.A.; Lobanov, P.D. Hydrodynamics and Heat Mass Transfer in Two-Phase Dispersed Flows in Pipes or Ducts. *Water* **2023**, *15*, 1969. [CrossRef]
29. Abdul Rahim, M.S.; Tajuddin, M.F.N.B.; Saad, M.S.; Hasanuzzaman, M.; Azmi, A.; Mohammed, M.F.B. Modeling, experimental investigation and real-time control of active water cooling system for photovoltaic module. *Energy Sources Part A Recovery Util. Environ. Eff.* **2024**, *46*, 3979–3995.
30. Brackbill, J.U.; Kothe, D.B.; Zemach, C. A continuum method for modeling surface tension. *J. Comput. Phys.* **1992**, *100*, 335–354. [CrossRef]
31. Li, X.; Xiang, L.; Wang, L.; Wang, Z.; Hu, Y. Experimental study on macroscopic and microscopic characteristics of flash boiling methanol spray under extremely cold conditions. *Energy Convers. Manag.* **2025**, *333*, 119780. [CrossRef]
32. Wang, Z.; Li, X.; Xiang, L.; Huang, Y.; Lang, B.; Cheng, X.; Zhang, J. Potential of kerosene-diesel blends as alternative fuels for diesel engines: Perspectives from spray combustion characteristics. *Fuel* **2023**, *335*, 127112. [CrossRef]
33. Agnihotri, S.N.; Raveshi, M.R.; Nosrati, R.; Bhardwaj, R.; Neild, A. Droplet splitting in microfluidics: A review. *Phys. Fluids* **2025**, *37*, 051304. [CrossRef]
34. Krištof, O.; Bulejko, P.; Svěrák, T. Experimental study on spray breakup in turbulent atomization using a spiral nozzle. *Processes* **2019**, *7*, 911. [CrossRef]
35. Ma, D.; Liang, D.; Zhu, C.; Fu, T.; Ma, Y.; Yuan, X.; Li, H.Z. The breakup dynamics and mechanism of viscous droplets in Y-shaped microchannels. *Chem. Eng. Sci.* **2021**, *231*, 116300. [CrossRef]
36. Gao, W.; Yu, C.; Yao, F. Droplets breakup via a splitting microchannel. *Chin. Phys. B* **2020**, *29*, 054702. [CrossRef]

https://doi.org/10.3390/en19122812